materials

MDPI

Article

$Cr_2P_2O_7$ as a Novel Anode Material for Sodium and Lithium Storage

Shuo Wang, Tianyuan Zhu, Fei Chen, Xiang Ding, Qiao Hu, Jiaying Liao, Xiaodong He and Chunhua Chen *

CAS Key Laboratory of Materials for Energy Conversions, Department of Materials Science and Engineering & Collaborative Innovation Center of Suzhou Nano Science and Technology, University of Science and Technology of China, Hefei 230026, China; ws14026@mail.ustc.edu.cn (S.W.); starzty@mail.ustc.edu.cn (T.Z.); chenf413@mail.ustc.edu.cn (F.C.); atp@mail.ustc.edu.cn (X.D.); huqiao@mail.ustc.edu.cn (Q.H.); ljy77@mail.ustc.edu.cn (J.L.); hxd427@mail.ustc.edu.cn (X.H.)

* Correspondence: cchchen@ustc.edu.cn

Received: 6 June 2020; Accepted: 10 July 2020; Published: 14 July 2020

Abstract: The development of new appropriate anode material with low cost is still main issue for sodium-ion batteries (SIBs) and lithium-ion batteries (LIBs). Here, $Cr_2P_2O_7$ with an in-situ formed carbon layer has been fabricated through a facile solid-state method and its storage performance in SIBs and LIBs has been reported first. The $Cr_2P_2O_7$@C delivers 238 mA h g^{-1} and 717 mA h g^{-1} at 0.05 A g^{-1} in SIBs and LIBs, respectively. A capacity of 194 mA h g^{-1} is achieved in SIBs after 300 cycles at 0.1 A g^{-1} with a high capacity retention of 92.4%. When tested in LIBs, 351 mA h g^{-1} is maintained after 600 cycles at 0.1 A g^{-1}. The carbon coating layer improves the conductivity and reduces the side reaction during the electrochemical process, and hence improves the rate performance and enhances the cyclic stability.

Keywords: chromium pyrophosphate; carbon coating; sodium ion battery; lithium ion battery

---

1. Introduction:

Lithium ion batteries (LIBs) have been widely used for portable electronic devices and electric vehicles now [1,2]. The limited lithium resource and the uneven global distribution become the major issues for their larger-scale manufacture [3–5]. Sodium-ion batteries (SIBs) are promising alternative for LIBs due to sodium's higher abundance, more even distribution and lower price compared to lithium [5]. For the materials choices, the larger ionic radius of Na^+ versus Li^+ (0.102 nm versus 0.076 nm) makes it impracticable to simply adopt most of the current anodes such as graphite for LIBs, exploration of appropriate anodes for SIBs is thus still necessary [6].

Nowadays the reported anode materials for SIBs mainly include carbon [7–9], alloys [10,11] and polyanion materials [12,13]. Among them, phosphate-based polyanionic materials have attracted enormous attention of the researchers due to their stable structural frameworks, in which there is a three-dimensional space for diffusion of the ions. In comparison with the metal oxides, transition metal polyanionic compounds usually demonstrate significant thermal stability as the strong covalent bonds between P and O can largely suppress the evolution of oxygen [5]. So far many polyanionic compounds such as $FePO_4$ and VPO_4 have been widely investigated as the anodes for LIBs [14–20]. However, quite few studies in literature have focused on the polyanionic compounds especially pyrophosphates as anode materials for SIBs. Wang et al. explored $NaTi_2(PO_4)_3$@C which delivers a capacity of 208 mA h g^{-1} [21], while Hu et al.

did a comparative study on layered TiP_2O_7 for Li/Na/K alkali metal batteries [22]. Fedotov et al. studied α-VPO_4 as a novel anode material which delivers a capacity of 80 mA h g^{-1} for SIBs [23]. It is also noticed that, compared with other anode materials for SIBs, $Cr_2P_2O_7$ shows advantages in materials cost as well as in electrochemical properties (Table 1).

Table 1. Cost and electrochemical properties (for SIBs) comparison of $Cr_2P_2O_7$ with other anode materials.

Anode Material	Raw Material	Raw Cost * (¥ kg^{-1})	Cycle Capability (mA h g^{-1})	Capacity (mA h g^{-1})	Ref.
$Cr_2P_2O_7$@C	$Cr(NO_3)_3{\cdot}9H_2O$ and Diammonium hydrogen phosphate	385	194 (300 cycles)	230 (100 mA g^{-1})	This work
$Na_4Ti_5O_{12}$/C	Sodium carbonate and Tetrabutyl titanate	680	81 (300 cycles)	92 (100 mA g^{-1})	[24]
$Mg_{0.5}Ti_2(PO_4)_3$@C	Magnesium acetate, Diammonium hydrogen phosphate and Titanium isopropoxide	520	130 (300 cycles)	200 (100 mA g^{-1})	[25]
$NaTi_2(PO_4)_3$/C	Sodium acetate, Tetrabutyl titanate and Phosphoric acid	609	170 (500 cycles)	208 (100 mA g^{-1})	[21]
MoS_2/C	Sodium molybdate dehydrate and Thiourea	758	352 (200 cycles)	400 (100 mA g^{-1})	[26]

* The costs are calculated based on the Aladin prices of the raw materials.

Although the effect of pressure on the structural behavior of $Cr_2P_2O_7$ was studied by Blanc et al. [27], it has never been investigated as an electrode material for batteries before. Considering the fact that phosphate-based polyanionic compounds always suffer from the poor electric conductivity which limits the electrochemical performance [28–35], it is necessary to apply a conducting carbon coating on the surface of the particles. For example, Kim et al. improved the rate capability and cycling stability of $Na_3V_2(PO_4)_3$ substantially through a carbon coating method [29]. The carbon coating can effectively improve the electrical conductivity, hence increasing the capacity and suppressing the capacity decay during cycling [36–40].

In this paper, we prepared the $Cr_2P_2O_7$ through a facile solid-state reaction and first reported the electrochemical performances of $Cr_2P_2O_7$ as anodes for LIBs and SIBs. In order to further investigate the influence of the surface modification, the carbon-coated sample $Cr_2P_2O_7$@C was synthesized by in-situ forming a carbon layer on the particles, and its electrochemical performances in LIBs and SIBs were also measured. The $Cr_2P_2O_7$@C shows a high capacity of 238 mA h g^{-1} at 0.05 A g^{-1} in SIBs. When measured in LIBs, it maintains 351 mA h g^{-1} after 600 cycles at 0.1 A g^{-1}.

2. Experimental Section

2.1. Synthesis of $Cr_2P_2O_7$ and $Cr_2P_2O_7$@C

Stoichiometric ratio of chromium nitrate ($Cr(NO_3)_3{\cdot}9H_2O$) and diammonium hydrogen phosphate ($(NH_4)_2HPO_4$) were dispersed in acetone and mixed by ball-milling for 10 h. The precursor was obtained after evaporating acetone at 110 °C in oven. Then it was sintered at 900 °C under argon atmosphere for 12 h to obtain $Cr_2P_2O_7$. To synthesize the carbon coated samples, 10, 20 and 40 wt% polyvinylpyrrolidone (PVP) (relative to the total mass of $Cr(NO_3)_3{\cdot}9H_2O$ and $(NH_4)_2HPO_4$) were added respectively into the mixture before ball-milling. The synthesized carbon coated samples were named as $Cr_2P_2O_7$-10PVP, $Cr_2P_2O_7$-20PVP, $Cr_2P_2O_7$-40PVP, respectively. The sample $Cr_2P_2O_7$-20PVP was also named as $Cr_2P_2O_7$@C.

2.2. Material Characterization

The phases and crystallinity of these products were characterized with an X-ray diffractometer (XRD, Rigaku TTR-III, Cu Kα radiation, Akishima, Tokyo, Japan. Their morphologies were observed by a scanning electron microscope (SEM, SIRION200, FEI, Hillsborough, OR, USA) or a transmission electron microscope (TEM, JEM-2100F, JEOL, Akishima, Tokyo, Japan). The elemental compositions were studied with energy-dispersive X-ray spectroscopy (EDS) equipped to the SEM instrument. Raman spectroscopy was performed by a Renishaw inVia Raman microscope (Gloucestershire, London, UK). The carbon content of $Cr_2P_2O_7$@C was analyzed with an infrared carbon-sulfur analyzer (CS8800C, Jinbo, Wuxi, China). DC electrical conductivity was measured by a direct volt-ampere method (STR722, Jingge, Suzhou, China), in which disc samples pressed at 20 kPa were contacted with a four-point probe.

2.3. Electrochemical Measurements

The electrochemical performances of the samples were tested using coin-type half cell (CR2032, Kejing, Hefei, China). The working electrodes were prepared by mixing $Cr_2P_2O_7$ or $Cr_2P_2O_7$@C (70%), acetylene black (20%) and poly(vinylidene fluoride) (10%) binder in N-methyl-2-pyrrolidinone. The slurries obtained were uniformly coated on a copper foil collector, followed by vacuum drying. The mass loading of the active material in electrodes was about 1.5 mg cm^{-2}. The lithium half cells were assembled in an argon-filled glovebox with lithium metal, Celgard 3501 polypropylene membrane (Celgard, Charlotte, NJ, USA) and 1 mol L^{-1} $LiPF_6$ in EC/DMC (1:1, *v*/*v*) as the counter electrode, separator and electrolyte, respectively. For sodium half cells, sodium metal was used as counter electrode with Whatman glass fiber and 1 mol L^{-1} $NaClO_4$ in EC/DMC (1:1, *v*/*v*) to which 1% fluoroethylene carbonate additive was added as the separator and electrolyte, respectively. The galvanostatic tests of the cells were conducted on a Neware BTS-610 multichannel battery test system (Neware Co., Shenzhen, China) in the voltage range of 0.1–3 V at room temperature (25 ± 2 °C). Cyclic voltammogram (CV) and electrochemical impedance spectroscopy (EIS) measurements were performed on a CHI660C electrochemical workstation (Chenhua Co., Shanghai, China). To measure the EIS spectrum, the batteries were activated at 50 mA g^{-1} for 2 cycles. The frequency range was from 10^5 to 10^{-2} Hz with an applied AC amplitude of 5 mV. The open circuit voltage of the cell was about 2.0 V.

3. Results and Discussion

Herein, we synthesize a green powder $Cr_2P_2O_7$ and the black carbon coated products through a facile solid-state reaction. All the peaks on their XRD patterns (Figure 1a) can be well indexed to the monoclinic structure (space group C2/c(15)), suggesting that both have high crystallinity and purity. Also, according to the SEM image of $Cr_2P_2O_7$@C (Figure 1b), it has micron-sized secondary particles of irregular shape with a size less than 2 μm, which are agglomerated with small grains of 200–500 nm. While the bare sample shows a quite different morphology with an average particle size over 8 μm (Figure S1a, Supporting Information). There are numerous pores in the bulk since the gases escaped quickly during the heating process. The HRTEM image of $Cr_2P_2O_7$@C (Figure 1e) shows the fine lattice fringes with a stripe distance of 0.433 nm, corresponding to the (002) plane of the monoclinic $Cr_2P_2O_7$. The HRTEM image of the bare sample (Figure S1b) shows a lattice fringe of 0.303 nm which corresponds to the (022) planes. The EDS results of $Cr_2P_2O_7$@C (Figure 1g) indicate a uniform distribution of the elements Cr, P, O and C. It further confirms the uniform carbon coating on the particles, which is of great benefit to the structural stability and the mitigation of the volume variation during cycling, therefore enhancing the electrochemical performance. The carbon coating layers with a thickness of 1–2, 3 and 5–6 nm can be observed clearly in $Cr_2P_2O_7$-10PVP, $Cr_2P_2O_7$-20PVP and $Cr_2P_2O_7$-40PVP (Figure 1d–f), respectively. The carbon content of $Cr_2P_2O_7$-10PVP, $Cr_2P_2O_7$-20PVP and $Cr_2P_2O_7$-40PVP analyzed by the infrared carbon-sulfur analyzer are 1.99 wt%, 6.85 wt% and 9.64 wt%, respectively. Furthermore, the Raman analysis confirms the presence of carbon (Figure 2a). Figure 2b shows the electronic conductivity of the carbon coated samples. The electronic conductivity of $Cr_2P_2O_7$ is less than 5×10^{-6} S cm^{-1} and out of the measurement lower limit of the instrument. But for the carbon coated samples, they display orders of magnitude increase in the electronic conductivity. The nitrogen sorption analysis shows type-IV curves (Figure 2c), and the corresponding specific surface areas are 124.1 m^2g^{-1} for $Cr_2P_2O_7$@C and 7.0 m^2g^{-1} for

$Cr_2P_2O_7$. The high surface area of $Cr_2P_2O_7$@C should have advantages in the transportation of Na^+ and the diffusion of electrolyte.

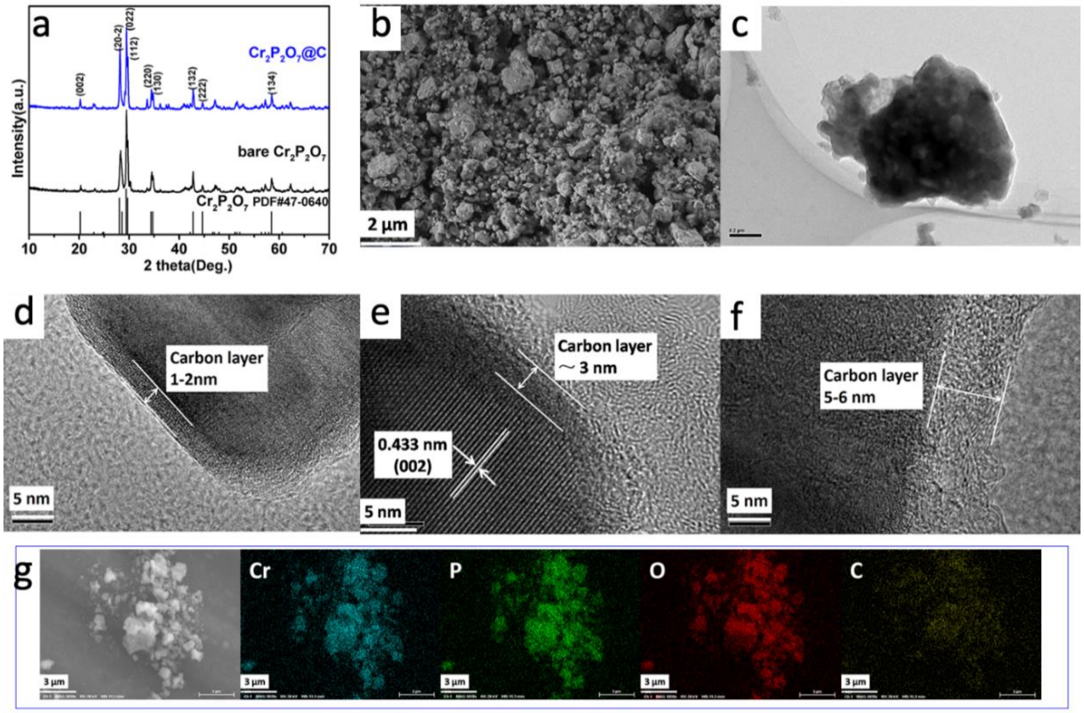

Figure 1. (**a**) XRD patterns of bare and carbon-coated $Cr_2P_2O_7$ samples; (**b**) SEM image and (**c**) TEM image of $Cr_2P_2O_7$@C. HRTEM images of (**d**) $Cr_2P_2O_7$-10PVP, (**e**) $Cr_2P_2O_7$-20PVP and (**f**) $Cr_2P_2O_7$-40PVP. (**g**) EDS elemental mapping of $Cr_2P_2O_7$@C.

The sodium storage performances of the two samples are measured. From the CV curves of $Cr_2P_2O_7$@C (Figure 2d), a sharp reduction peak below 0.2 V can be observed obviously in the initial cathodic process, corresponding to the formation of the solid electrolyte interface (SEI) layer. There are also two peaks at 0.7 V and 1.2 V, assigned to the conversion reaction. For the anodic process, a broad oxidation peak at 1.5 V is observed which can be assigned to backward conversion reaction. Furthermore, the curves of the subsequent cycles almost overlap with each other, suggesting the high stability and reversibility of $Cr_2P_2O_7$@C, which are in contrast with the bare $Cr_2P_2O_7$ (Figure S2). The discharge-charge profiles of $Cr_2P_2O_7$@C (Figure 3c) are consistent with the CV results. The first-cycle charge capacity of $Cr_2P_2O_7$-10PVP (Figure 3b), $Cr_2P_2O_7$-20PVP and $Cr_2P_2O_7$-40PVP (Figure 3d) reaches 199, 238 and 196 mA h g^{-1} at 0.05 A g^{-1}, respectively. While it is only 142 mA h g^{-1} for bare $Cr_2P_2O_7$ (Figure 3a). The increased capacity can be ascribed to the presence of the conductive carbon layer which can facilitate the conduction of electrons and help the sodium ions reach the inner cores of the particles. Obviously, $Cr_2P_2O_7$-20PVP is the optimal sample.

When increasing the current rate (Figure 4a), $Cr_2P_2O_7$@C delivers excellent rate capacities of 230, 213, 182, 152, 121, 64, 22 mA h g^{-1} at different current densities of 0.1, 0.2, 0.5, 1.0, 2.0, 5.0, 10.0 A g^{-1}, respectively. A capacity of 232 mA h g^{-1} can be achieved when returning to 0.1 A g^{-1} with no capacity decrease, indicating the high reversibility and good rate tolerance with the help of the in-situ formed carbon layer. As a comparison for the bare $Cr_2P_2O_7$ (Figure 4b), lower capacities of 99, 55, 15 mA h g^{-1} are achieved at 0.1, 0.2, 0.5 A g^{-1}, respectively, with ignorable capacity at higher current densities. When returning to 0.1 A g^{-1}, it maintains only 63 mA h g^{-1} with a quite large capacity loss, suggesting a poor stability during the electrochemical process. As shown in Figure 4c,d, the cycling performances of the materials in Na/$Cr_2P_2O_7$ cells were also tested. After 300 cycles at 0.1 A g^{-1}, a capacity of 194 mA h g^{-1} is achieved with a high capacity retention of 92.4% for $Cr_2P_2O_7$@C, while the bare $Cr_2P_2O_7$ maintains a much lower capacity of 20 mA h g^{-1}. After coated with a conductive carbon layer which can facilitate the conduction of electrons, $Cr_2P_2O_7$@C also has smaller particle size with a microporous structure. The micro-porosity and higher specific area increase the contact area between material and electrolyte and shorten the path of ion diffusion. The carbon coating also reduces the direct contact between the material and the electrolyte and reducing the side reaction, which has a major impact on the improvement of cycle performance. And the volume expansion of the material can be alleviated to a certain extent. Therefore, the capacity and cyclability of the material are improved. When compared with other widely reported anode materials, the electrochemical properties of $Cr_2P_2O_7$@C are also competitive (Table 1).

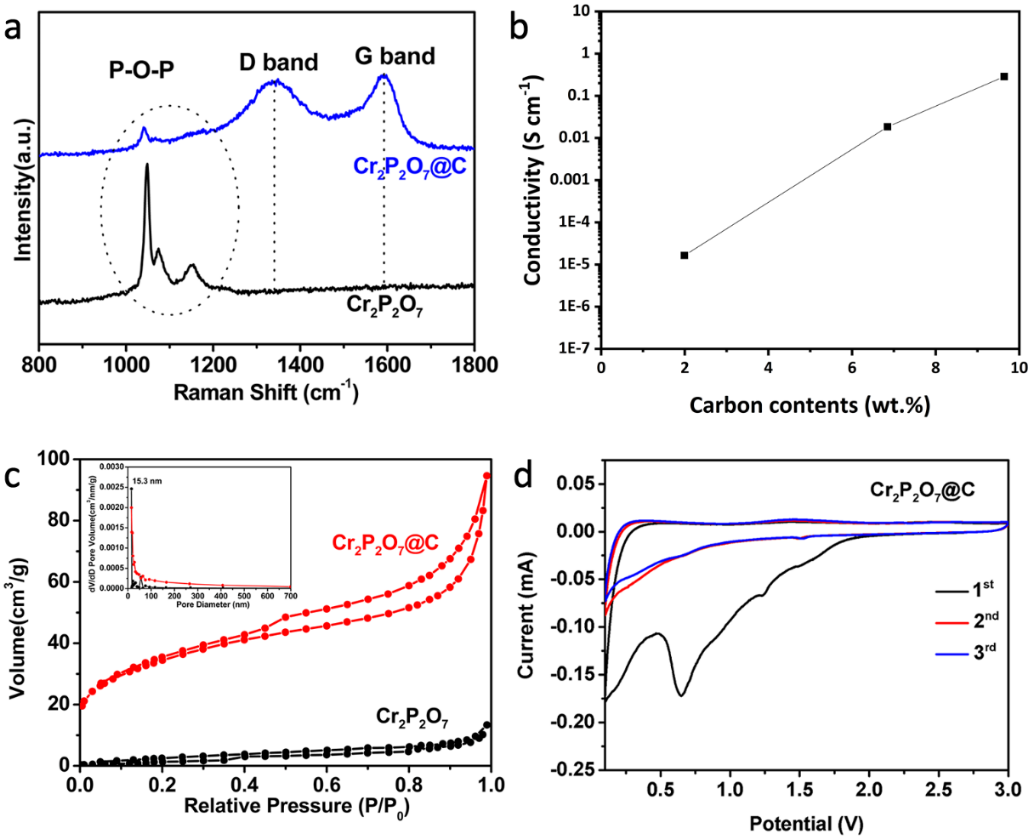

Figure 2. (**a**) Raman spectra of $Cr_2P_2O_7$@C and $Cr_2P_2O_7$; (**b**) Electronic conductivity of the carbon coated samples; (**c**) N_2 adsorption-desorption isotherms and (inset) the pore size distribution curves of $Cr_2P_2O_7$@C and $Cr_2P_2O_7$; (**d**) CV curves in SIBs of $Cr_2P_2O_7$@C in the first 3 cycles between 0 V and 3 V at a scanning rate of 0.1 mV s^{-1}.

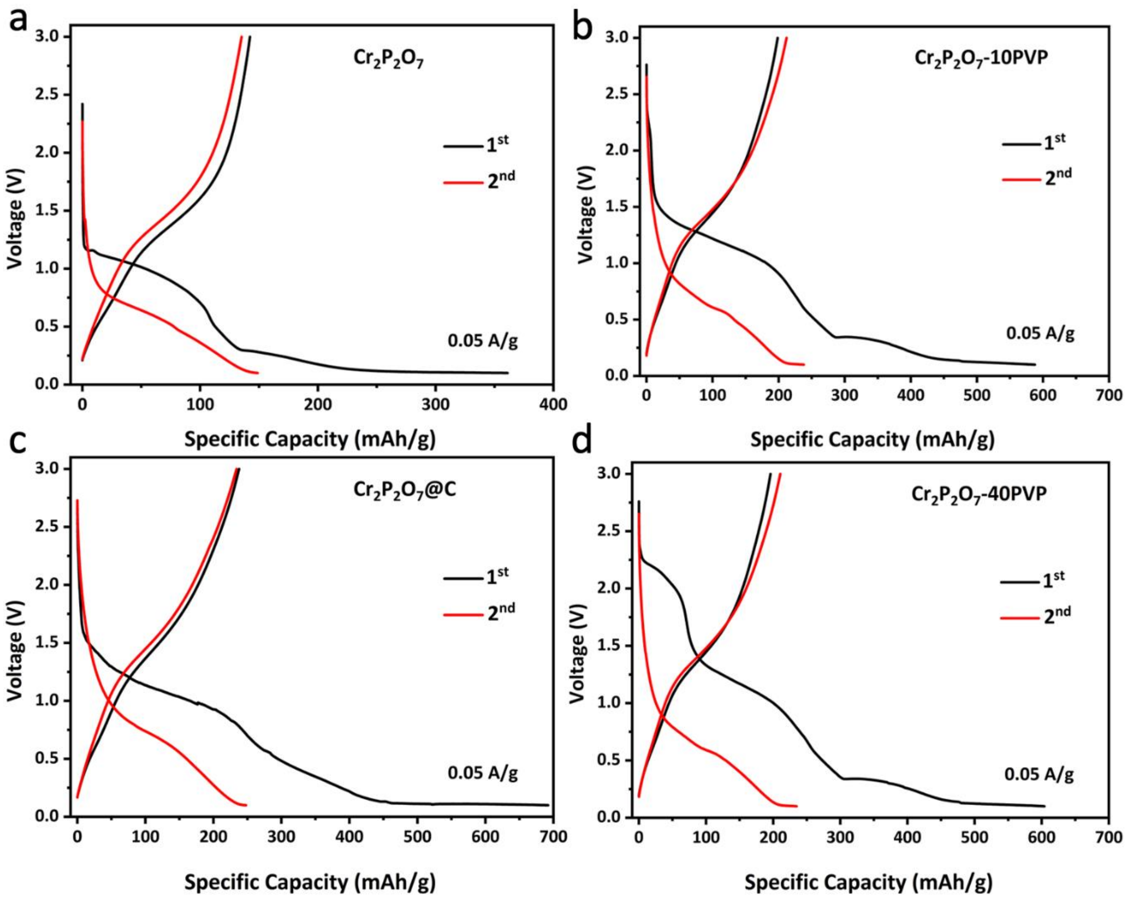

Figure 3. Charge-discharge profiles of (**a**) $Cr_2P_2O_7$, (**b**) $Cr_2P_2O_7$-10PVP, (**c**) $Cr_2P_2O_7$-20PVP ($Cr_2P_2O_7$@C) and (**d**) $Cr_2P_2O_7$-40PVP for the initial 2 cycles in Na/$Cr_2P_2O_7$ cells at 0.05 A g^{-1}.

As a new anode material, the lithium storage performance of $Cr_2P_2O_7$@C is also investigated. On its CV curves (Figure 5a), a sharp reduction peak at 0.2 V is observed which corresponds to the formation of the SEI layer in the initial cathodic process. There are also two minor peaks at 0.6 V and 1.7 V assigned to the conversion reaction. The anodic curves show two corresponding oxidation peaks at 1.0 V and 1.9 V. The CV curves of $Cr_2P_2O_7$ show the same characteristics (Figure S3). On the charge-discharge voltage profiles of $Cr_2P_2O_7$@C (Figure 5b), two plateaus at 0.6 V and 1.7 V in the first discharge and two plateaus at 1.0 V and 1.9 V in the charge profile are measured, which correspond exactly to the CV curves. Hence we propose following conversion reaction based on the charge/discharge profiles and the CV curves:

$$4A^{+} + 4e^{-} + Cr_2P_2O_7 \frac{Discharge}{Charge} 2Cr + A_4P_2O_7 \ (A : Li, Na)$$

The initial charge capacity for $Cr_2P_2O_7$@C in Li/$Cr_2P_2O_7$ cells is 717 mA h g^{-1} at 0.05 A g^{-1}, while it is only 517 mA h g^{-1} for $Cr_2P_2O_7$ (Figure S4). The rate performance of $Cr_2P_2O_7$@C is also markedly better than $Cr_2P_2O_7$ (Figure 5c,d). The former shows capacities of 285 and 184 mA h g^{-1} at current densities of 5.0 and 10.0 A g^{-1}, respectively, while the latter shows little capacity at these rates. It is further demonstrated that the in-situ fabricated carbon coating can effectively improve the electrochemical performance. For the cycling properties (Figure 5e,f), $Cr_2P_2O_7$@C maintains a reversible capacity of 351 mA h g^{-1} after 600 cycles at 0.1 A g^{-1}, which is much higher than that of the bare $Cr_2P_2O_7$ with a capacity down to 223 mA h g^{-1} after 235 cycles. Note that the rapid decrease in the first dozen cycles of both samples may be due to the initial activation process.

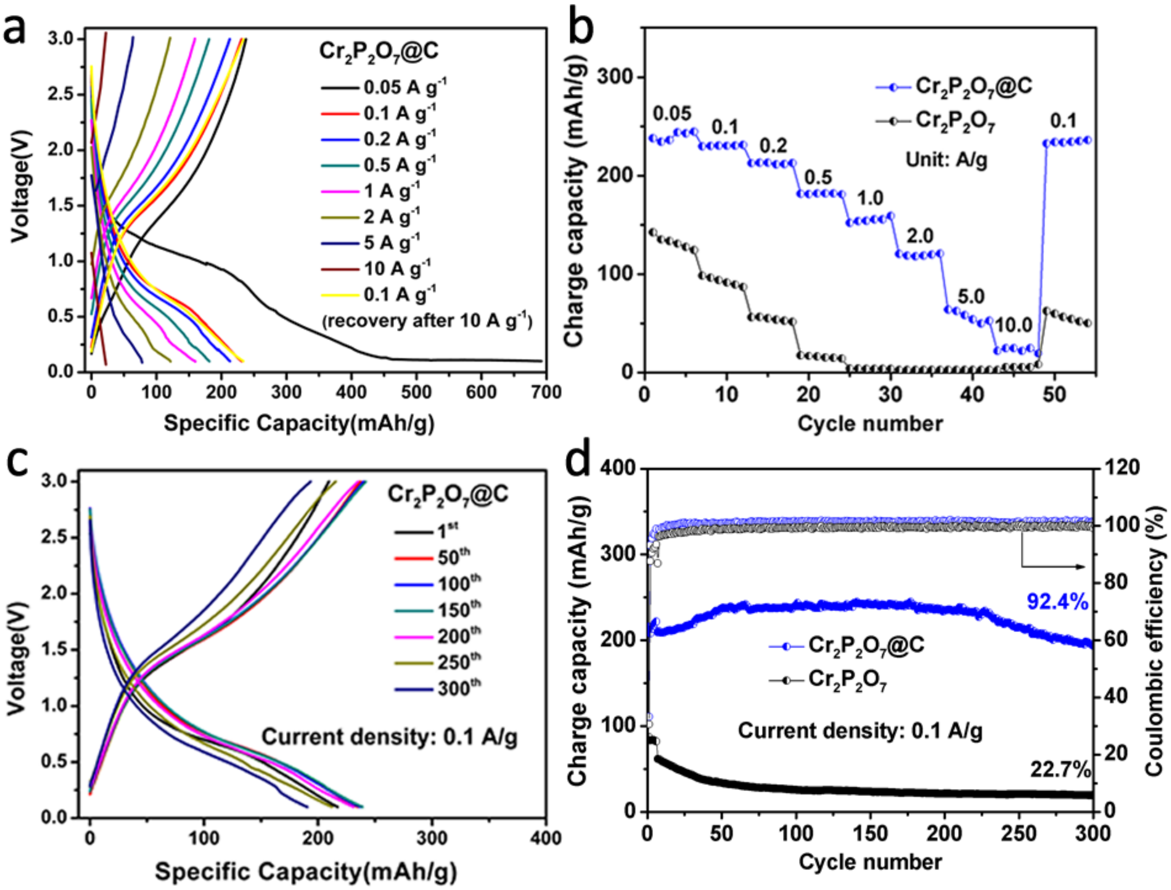

Figure 4. Electrochemical performance in Na/$Cr_2P_2O_7$ cells: charge-discharge profiles of different current densities (**a**); comparison of the rate performances (**b**); charge-discharge curves of the selected cycles of $Cr_2P_2O_7$@C at 0.1 A g^{-1} (**c**); comparison of the cycling performances (**d**). The cells were initially activated for three times at a low current density of 0.05 A g^{-1} and then cycled at 0.1 A g^{-1}.

The electrochemical impedance spectroscopy (EIS) test was measured in both Li/$Cr_2P_2O_7$ and Na/$Cr_2P_2O_7$ cells to study the electrochemical kinetics (Figure 6). $Cr_2P_2O_7$@C exhibits lower charge transfer resistance and electrolyte resistance than the bare $Cr_2P_2O_7$ in both cases (Tables 2 and 3). Due to the incorporation of the carbon layer, the calculated apparent lithium diffusion coefficient and apparent sodium diffusion coefficient of $Cr_2P_2O_7$@C are 2.7×10^{-12} cm^2 s^{-1} and 2.3×10^{-12} cm^2 s^{-1}, respectively, which are higher than those of $Cr_2P_2O_7$ (5.1×10^{-14} cm^2 s^{-1} and 3.0×10^{-14} cm^2 s^{-1}). Such a huge difference in apparent diffusion coefficient is mainly due to the difference in specific area (124.1 m^2g^{-1} for $Cr_2P_2O_7$@C vs. 7.0 m^2g^{-1} for $Cr_2P_2O_7$) because the area used to calculate the diffusion coefficient is the geometric area which is much less than the real contact area between the electrode and the liquid electrolyte. Thus the in-situ carbon coating method efficiently improves the cycle and rate performances of lithium and sodium cells.

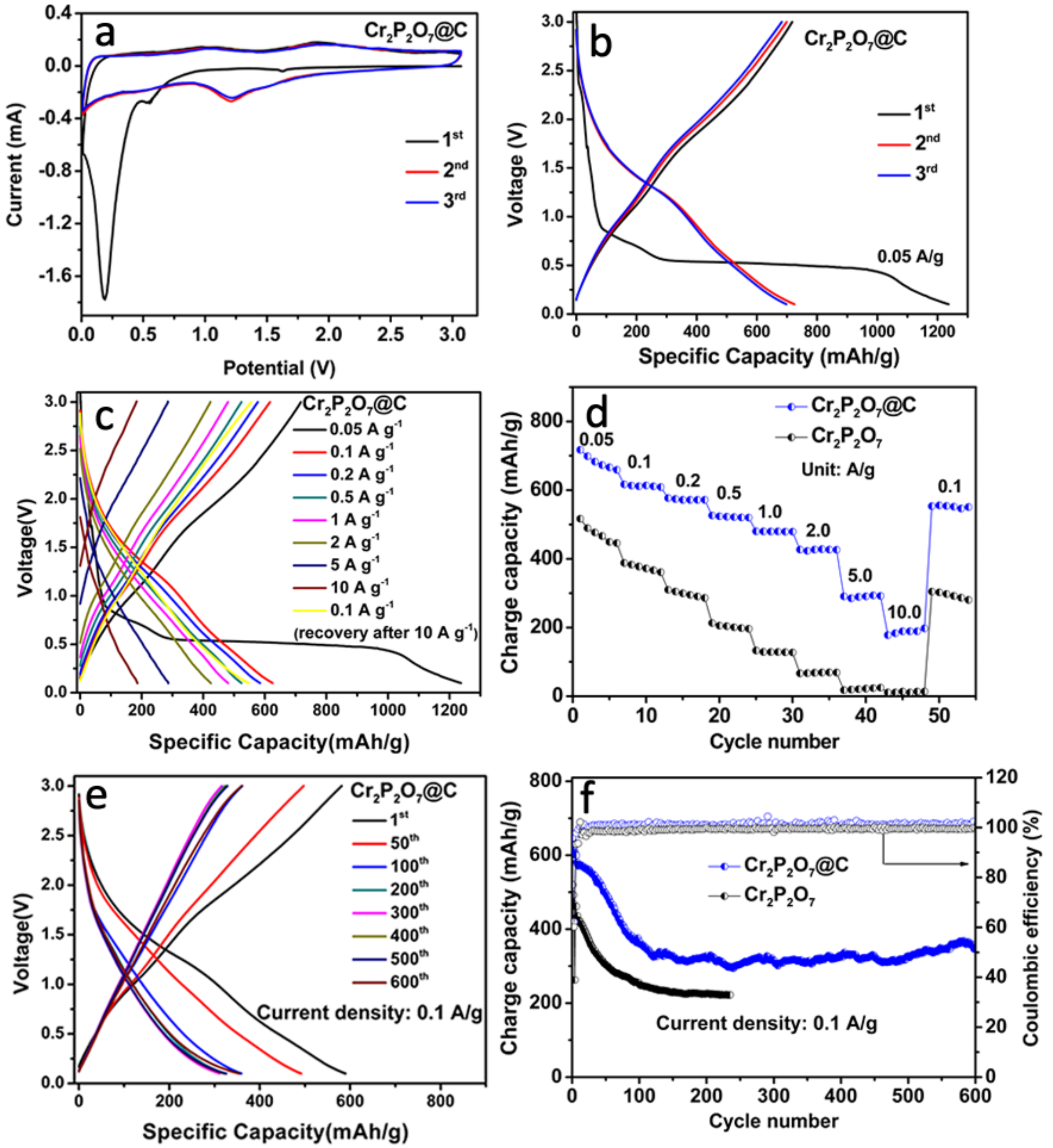

Figure 5. Electrochemical performance in Li/$Cr_2P_2O_7$ cells: CV curves of $Cr_2P_2O_7$@C in the first 3 cycles between 0 V and 3 V at a scanning rate of 0.1 mV s^{-1} (**a**); charge-discharge profiles for the initial 3 cycles (**b**); charge-discharge profiles of different current densities (**c**); comparison of the rate performances (**d**); charge-discharge curves of the selected cycles of $Cr_2P_2O_7$@C at 0.1 A g^{-1} (**e**); comparison of the cycling performances (**f**). The cells were initially activated for three times at a low current density of 0.05 A g^{-1} and then cycled at 0.1 A g^{-1}.

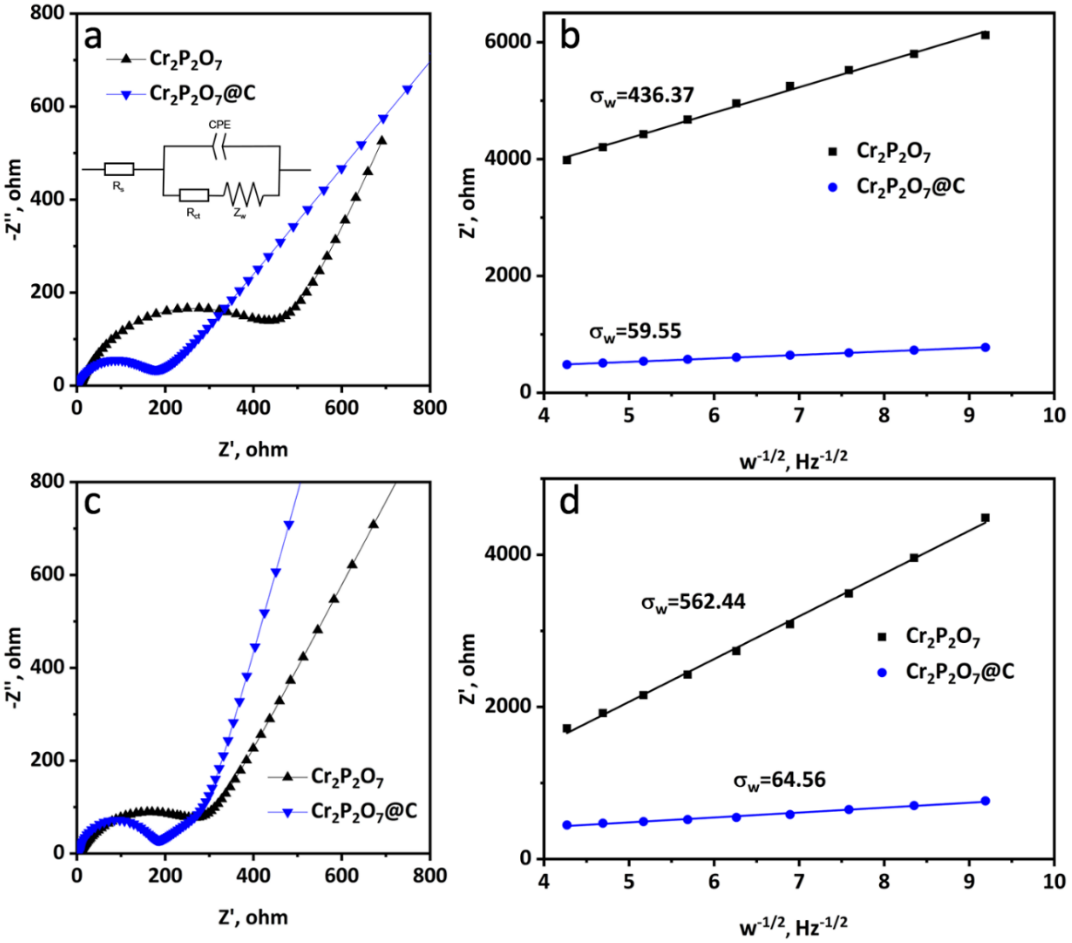

Figure 6. The fitting impedance spectra of $Cr_2P_2O_7$@C and $Cr_2P_2O_7$ in (**a**) Li/$Cr_2P_2O_7$ and (**b**) Na/$Cr_2P_2O_7$ cells. The equivalent circuit used for fitting the experimental EIS data of Li/$Cr_2P_2O_7$ and Na/$Cr_2P_2O_7$ cells (inset). Linear fitting to Z′ versus $\omega^{-1/2}$ plots in the low-frequency range in (**c**) Li/$Cr_2P_2O_7$ and (**d**) Na/$Cr_2P_2O_7$ cells.

Table 2. Results of electrochemical impedance and Warburg coefficient of $Cr_2P_2O_7$ in Li/$Cr_2P_2O_7$ cell.

Samples	**R_s, Ω**	**R_{ct}, Ω**	**σ_w, Ω s^{-1}**	**D_{Na^+}, cm^2 s^{-1}**
$Cr_2P_2O_7$	10.5	466.2	436.4	5.1×10^{-14}
$Cr_2P_2O_7$@C	5.7	131.6	59.6	2.7×10^{-12}

Table 3. Results of electrochemical impedance and Warburg coefficient of of $Cr_2P_2O_7$ in Na/$Cr_2P_2O_7$ cell.

Samples	**R_s, Ω**	**R_{ct}, Ω**	**σ_w, Ω s^{-1}**	**D_{Li^+}, cm^2 s^{-1}**
$Cr_2P_2O_7$	8.6	303.7	562.4	3.0×10^{-14}
$Cr_2P_2O_7$@C	5.3	159.2	64.6	2.3×10^{-12}

4. Conclusions

To explore new anode materials for LIBs and SIBs, a pyrophosphate powder, i.e., $Cr_2P_2O_7$, is synthesized via a facile solid-state reaction method. An in-situ carbon coating strategy is also taken to enhance its electronic conductivity and thus the apparent alkali ion diffusion coefficient. Such an anode material exhibits good electrochemical properties both in rate and cycling performances in LIBs and SIBs. The in-situ carbon layer is very important for the improvement compared to the non-coated samples. This novel phosphate-based anode material is also expected to promote the overall safety of the batteries.

Supplementary Materials: The following are available online at http://www.mdpi.com/1996-1944/13/14/3139/s1, Figure S1. SEM image (a) and TEM image (b) of $Cr_2P_2O_7$. Figure S2. The CV curves of $Cr_2P_2O_7$ in the first 3 cycles between 0 V and 3 V at a scanning rate of 0.1 mV s^{-1} in SIBs. Figure S3. The CV curves of $Cr_2P_2O_7$ in the first 3 cycles between 0 V and 3 V at a scanning rate of 0.1 mV s^{-1} in LIBs. Figure S4. The charge-discharge profiles of $Cr_2P_2O_7$ for the initial 3 cycles in LIBs.

Author Contributions: Conceptualization, S.W.; methodology, S.W., T.Z., F.C. and X.D.; software, S.W.; validation, S.W., T.Z., J.L. and F.C.; formal analysis, S.W., T.Z., Q.H. and F.C.; investigation, S.W., T.Z. and F.C.; resources, S.W., X.D., Q.H. and J.L.; data curation, S.W.; writing—original draft preparation, S.W.; writing—review and editing, S.W. and C.C.; visualization, X.H.; supervision, C.C.; project administration, C.C.; funding acquisition, C.C. All authors have read and agreed to the published version of the manuscript.

Funding: This research was funded by the National Science Foundation of China grant number NSAF U1630106, 21875237, 51577175 and National Key R&D Program of China grant number 2018YFB0905400.

Conflicts of Interest: There are no conflicts to declare.

References

1. Dresselhaus, M.S.; Thomas, I.L. Alternative energy technologies. *Nature* **2001**, *414*, 332. [CrossRef] [PubMed]
2. Dunn, B.; Kamath, H.; Tarascon, J.-M. Electrical energy storage for the grid: A battery of choices. *Science* **2011**, *334*, 928. [CrossRef] [PubMed]
3. Tarascon, J.M.; Armand, M. Issues and challenges facing rechargeable lithium batteries. *Nature* **2001**, *414*, 359. [CrossRef] [PubMed]
4. Slater, M.D.; Kim, D.; Lee, E.; Johnson, C.S. Sodium-ion batteries. *Adv. Funct. Mater.* **2013**, *23*, 947. [CrossRef]
5. Hwang, J.-Y.; Myung, S.-T.; Sun, Y.-K. Sodium-ion batteries: Present and future. *Chem. Soc. Rev.* **2017**, *46*, 3529. [PubMed]
6. Perveen, T.; Siddiq, M.; Shahzad, N.; Ihsan, R.; Ahmad, A.; Shahzad, M.I. Prospects in anode materials for sodium ion batteries–A review. *Renew. Sustain. Energy Rev.* **2020**, *119*, 30. [CrossRef]
7. Xia, J.-L.; Yan, D.; Guo, L.-P.; Dong, X.-L.; Li, W.-C.; Lu, A.-H. Hard carbon nanosheets with uniform ultramicropores and accessible functional groups showing high realistic capacity and superior rate performance for sodium-ion storage. *Adv. Mater.* **2020**, *32*, 21. [CrossRef]
8. Wei, R.C.; Huang, M.; Ma, W.Z.; Xi, B.J.; Feng, Z.Y.; Li, H.B.; Feng, J.K.; Xiong, S.L. N-doped carbon nanotubes formed in a wide range of temperature and ramping rate for fast sodium storage. *J. Energy Chem.* **2020**, *49*, 136. [CrossRef]
9. Zhang, W.C.; Lan, C.W.; Xie, X.H.; Cao, Q.Y.; Zheng, M.T.; Dong, H.W.; Hu, H.; Xiao, Y.; Liu, Y.L.; Liang, Y.R. Facile construction of hollow carbon nanosphere-interconnected network for advanced sodium-ion battery anode. *J. Colloid Interface Sci.* **2019**, *546*, 53. [CrossRef]
10. Yang, K.; Tang, J.; Liu, Y.; Kong, M.; Zhou, B.; Shang, Y.; Zhang, W.-H. Controllable synthesis of peapod-like Sb@C and corn-like C@Sb nanotubes for sodium storage. *ACS Nano* **2020**, *14*, 5728. [CrossRef]
11. Liu, M.Y.; Huang, J.F.; Li, J.L.; Cao, L.Y.; Zhao, Y.X.; Ma, M.; Koji, K. Manipulating the stress of Sn in carbon structure to realize long-life high performance sodium ion battery anode material. *J. Alloys Compd.* **2020**, *834*, 9. [CrossRef]
12. Zheng, W.G.; Wu, M.; Yang, C.; Tang, Z.G.; Hu, H.N. Carbon nanotube linked $NaTi_2(PO_4)_3/C$ composite with three-dimensional conductive network as superior electrode for sodium ion battery. *Ionics* **2020**, *26*, 2883. [CrossRef]
13. Jian, Z.; Sun, Y.; Ji, X. A new low-voltage plateau of $Na_3V_2(PO_4)_3$ as an anode for Na-ion batteries. *Chem. Commun.* **2015**, *51*, 6381. [CrossRef]

14. Zhang, B.; Han, Y.-D.; Zheng, J.-C.; Zhang, J.-F.; Shen, C.; Ming, L.; Yuan, X.-B.; Li, H. $VOPO_4$ nanosheets as anode materials for lithium-ion batteries. *Chem. Commun.* **2014**, *50*, 11132. [CrossRef]
15. Zheng, J.-C.; Han, Y.-D.; Zhang, B.; Shen, C.; Ming, L.; Ou, X.; Zhang, J.-F. Electrochemical properties of VPO_4/C nanosheets and microspheres as anode materials for lithium-ion batteries. *ACS Appl. Mater. Interfaces* **2014**, *6*, 6223. [CrossRef]
16. Nan, X.; Liu, C.; Zhang, C.; Ma, W.; Wang, K.; Li, Z.; Cao, G. A new anode material for high performance lithium-ion batteries: $V_2(PO_4)O$/C. *J. Mater. Chem. A* **2016**, *4*, 9789. [CrossRef]
17. Yang, Y.; Wang, B.; Zhu, J.; Zhou, J.; Xu, Z.; Fan, L.; Zhu, J.; Podila, R.; Rao, A.M.; Lu, B. Bacteria absorption-based $Mn_2P_2O_7$–carbon@reduced graphene oxides for high-performance lithium-ion battery anodes. *ACS Nano* **2016**, *10*, 5516. [CrossRef]
18. Wen, Y.; Chen, L.; Pang, Y.; Guo, Z.; Bin, D.; Wang, Y.-G.; Wang, C.; Xia, Y. TiP_2O_7 and expanded graphite nanocomposite as anode material for aqueous lithium-ion batteries. *ACS Appl. Mater. Interfaces* **2017**, *9*, 8075. [CrossRef] [PubMed]
19. Zhao, D.; Meng, T.; Qin, J.W.; Wang, W.; Yin, Z.G.; Cao, M.H. Rational construction of multivoids-assembled hybrid nanospheres based on VPO_4 encapsulated in porous carbon with superior lithium storage performance. *ACS Appl. Mater. Interfaces* **2017**, *9*, 1437. [CrossRef] [PubMed]
20. Liao, C.Y.; Wen, Y.W.; Xia, Z.G.; Qin, R.H.; Liu, X.; Yu, Y.; Shan, B.; Zhai, T.Y.; Li, H.Q. Si-doping mediated phase control from beta- to gamma-form Li_3VO_4 toward smoothing Li insertion/extraction. *Adv. Energy Mater.* **2018**, *8*, 8. [CrossRef]
21. Wang, D.; Liu, Q.; Chen, C.; Li, M.; Meng, X.; Bie, X.; Wei, Y.; Huang, Y.; Du, F.; Wang, C.; et al. NASICON-structured $NaTi_2(PO_4)_3$@C nanocomposite as the low operation-voltage anode material for high-performance sodium-ion batteries. *ACS Appl. Mater. Interfaces* **2016**, *8*, 2238. [CrossRef] [PubMed]
22. Hu, Q.; Liang, J.-Y.; Liao, J.-Y.; Tang, Z.-F.; Ding, X.; Chen, C.-H. A comparative study on nanocrystalline layered and crystalline cubic TiP_2O_7 for rechargeable Li/Na/K alkali metal batteries. *J. Mater. Chem. A* **2018**, *6*, 15230. [CrossRef]
23. Fedotov, S.S.; Samarin, A.S.; Nikitina, V.A.; Stevenson, K.J.; Abakumov, A.M.; Antipov, E.V. α-VPO_4: A Novel Many Monovalent Ion Intercalation Anode Material for Metal-Ion Batteries. *ACS Appl. Mater. Interfaces* **2019**, *11*, 12431. [CrossRef] [PubMed]
24. Tang, Y.K.; Liu, L.; Zhang, Y.; Zhao, H.Y.; Kong, L.B.; Gao, S.S. Confined formation of monoclinic $Na_4Ti_5O_{12}$ nanoparticles embedded into porous CNTs: Towards enhanced electrochemical performances for sodium ion batteries. *New J. Chem.* **2018**, *42*, 19340. [CrossRef]
25. Zhao, Y.; Wei, Z.; Pang, Q.; Wei, Y.; Cai, Y.; Fu, Q.; Du, F.; Sarapulova, A.; Ehrenberg, H.; Liu, B.; et al. NASICON-type $Mg_{0.5}Ti_2(PO_4)_3$ negative electrode material exhibits different electrochemical energy storage mechanisms in Na-ion and Li-Ion batteries. *ACS Appl. Mater. Interfaces* **2017**, *9*, 4709. [CrossRef]
26. Yao, Z.R.; Zhu, K.J.; Li, X.; Wang, J.; Yan, K.; Liu, J.S. Interlayer-expanded MoS_2 nanosheets/nitrogen-doped carbon as a high-performance anode for sodium -ion batteries. *J. Alloys Compd.* **2020**, *838*, 9. [CrossRef]
27. Blanc, N.A.; Williams, Q.; El Bali, B.; Essehli, R. A vibrational study of phase transitions in $Fe_2P_2O_7$ and $Cr_2P_2O_7$ under high-pressures. *J. Am. Ceram. Soc.* **2018**, *101*, 5257. [CrossRef]
28. Liang, X.; Ou, X.; Dai, H.; Zheng, F.; Pan, Q.; Liu, P.; Xiong, X.; Liu, M.; Yang, C. Exploration of VPO_4 as a new anode material for sodium-ion batteries. *Chem. Commun.* **2017**, *53*, 12696. [CrossRef]
29. Kim, H.; Lim, H.; Kim, H.-S.; Kim, K.J.; Byun, D.; Choi, W. Polydopamine-derived N-doped carbon-wrapped $Na_3V_2(PO_4)_3$ cathode with superior rate capability and cycling stability for sodium-ion batteries. *Nano Res.* **2019**, *12*, 397. [CrossRef]
30. Mizuno, Y.; Kotobuki, M.; Munakata, H.; Kanamura, K. Effect of carbon source on electrochemical performance of carbon coated $LiMnPO_4$ cathode. *J. Ceram. Soc. Jpn.* **2009**, *117*, 1225. [CrossRef]
31. Huo, H.; Lin, Z.Y.; Wu, D.; Zhong, G.M.; Shao, J.Y.; Xu, X.; Xie, B.X.; Ma, Y.L.; Dai, C.S.; Du, C.Y.; et al. Investigating the structure of an active material-carbon interface in the monoclinic $Li_3V_2(PO_4)_3$/C composite cathode. *ACS Appl. Energy Mater.* **2019**, *2*, 3692. [CrossRef]

32. Kim, H.J.; Bae, G.H.; Lee, S.M.; Ahn, J.H.; Kim, J.K. Properties of lithium iron phosphate prepared by biomass-derived carbon coating for flexible lithium ion batteries. *Electrochim. Acta* **2019**, *300*, 18. [CrossRef]
33. Galceran, M.; Guerfi, A.; Armand, M.; Zaghib, K.; Casas-Cabanas, M. The critical role of carbon in the chemical delithiation kinetics of $LiFePO_4$. *J. Electrochem. Soc.* **2020**, *167*, 3. [CrossRef]
34. Wang, Q.; Luo, Y.; Gu, F.; Shui, M.; Shu, J. The preparation, characterization, electro-chemical performance and transporting mechanism of $Na_{1.25}Cr_{0.25}Ti_{1.75}(PO_4)_3/C$ as anode material for SIBs. *Solid State Ionics* **2020**, *352*, 115368. [CrossRef]
35. Alfaruqi, M.H.; Islam, S.; Song, J.; Kim, S.; Pham, D.T.; Jo, J.; Kim, S.; Baboo, J.P.; Putro, D.Y.; Mathew, V.; et al. Carbon-coated rhombohedral $Li_2NaV_2(PO_4)_3$ nanoflake cathode for Li-ion battery with excellent cycleability and rate capability. *Chem. Phys. Lett.* **2017**, *681*, 44. [CrossRef]
36. Song, J.; Park, S.; Kim, S.; Mathew, V.; Alfaruqi, M.H.; Jo, J.; Kim, J. Uniform Carbon Coated $Na_3V_2(PO_4)_2O_{2x}F_{3-2x}$ Nanoparticles for Sodium Ion Batteries as Cathode. *ACS Sustain. Chem. Eng.* **2019**, *7*, 18826. [CrossRef]
37. Kumar, P.R.; Yahia, H.B.; Belharouak, I.; Sougrati, M.T.; Passerini, S.; Amin, R.; Essehli, R. Electrochemical investigations of high-voltage $Na_4Ni_3(PO_4)_2P_2O_7$ cathode for sodium-ion batteries. *J. Solid State Electrochem.* **2020**, *24*, 17. [CrossRef]
38. Kumar, P.R.; Essehli, R.; Yahia, H.B.; Amin, R.; Belharouak, I. Electrochemical studies of a high voltage $Na_4Co_3(PO_4)_2P_2O_7$-MWCNT composite through a selected stable electrolyte. *RSC Adv.* **2020**, *10*, 15983. [CrossRef]
39. Criado, A.; Lavela, P.; Ortiz, G.; Tirado, J.L.; Perez-Vicente, C.; Bahrou, N.; Edfouf, Z. Highly dispersed oleic-induced nanometric $C@Na_3V_2(PO_4)_2F_3$ composites for efficient Na-ion batteries. *Electrochim. Acta* **2020**, *332*, 8. [CrossRef]
40. Kumar, P.R.; Kheireddine, A.; Nisar, U.; Shakoor, R.A.; Essehli, R.; Amin, R.; Belharouak, I. $Na_4MnV(PO_4)_3$-rGO as Advanced cathode for aqueous and non-aqueous sodium ion batteries. *J. Power Sources* **2019**, *429*, 149. [CrossRef]

© 2020 by the authors. Licensee MDPI, Basel, Switzerland. This article is an open access article distributed under the terms and conditions of the Creative Commons Attribution (CC BY) license (http://creativecommons.org/licenses/by/4.0/).